

1 Magmatic-tectonic conditions for hydrothermal venting on
2 an ultraslow-spread oceanic core complex

3 **Jennifer L. Harding¹, Harm J.A. Van Avendonk¹, Nicholas W. Hayman¹, Ingo**
4 **Grevenmeyer², Christine Peirce³, and Anke Dannowski²**

5 *¹Institute for Geophysics, Jackson School of Geosciences, University of Texas at Austin,*
6 *J.J. Pickle Research Campus, 10100 Burnet Road, Building 196, Austin, Texas 78758,*
7 *USA*

8 *²GEOMAR Helmholtz Centre of Ocean Research, Wischhofstr. 1-3, D-24148 Kiel,*
9 *Germany*

10 *³Department of Earth Sciences, University of Durham, South Road, Durham DH1 3LE,*
11 *UK*

12 **ABSTRACT**

13 Hydrothermal venting, an important cooling mechanism of the Earth, supports a
14 diverse array of seafloor and sub-seafloor ecosystems that are sustained by large thermal
15 and chemical fluxes. Vents have been found along even the slowest and coldest spreading
16 centers, calling into question the driving heat source for these vents. The ultraslow-
17 spreading Mid-Cayman Spreading Center in the Caribbean Sea, which hosts the axial-
18 flank Von Damm Vent Field (VDVF), provides an opportunity to probe the mechanisms
19 for venting at ultraslow spreading rates. Using active-source seismic data from the 2015
20 CaySeis experiment, we determined the seismic velocities in the large massif beneath the
21 VDVF. We propose that this massif was produced by a pulse of on-axis magmatism ~2
22 Mya, which was then followed by exhumation, cooling, and fracturing. A low seismic

23 velocity anomaly 5 km below the VDVF is evidence for either a cracking front mining
24 lithospheric heat or intrusive magmatic sills, both of which could drive ongoing deep
25 hydrothermal fluid circulation. We conclude that the transient magmatism and variable
26 crustal thickness at ultraslow-spreading centers create conditions for long-lived
27 hydrothermal venting that may be widespread, and other VDVF-like vents may be
28 common in these areas.

29 INTRODUCTION

30 Mid-ocean ridge hydrothermal vents display a wide range of thermal and
31 chemical properties that support diverse, extremophile communities (e.g., Kelley et al.,
32 2002). The most numerous mid-ocean ridge vents occur along faster-spreading, hotter
33 ridges, which spread at full-rates of $> 75 \text{ mm yr}^{-1}$ from axes with depths shallower than
34 4000 mbsl (meters below sea-level) and accrete oceanic crust of a relatively uniform,
35 symmetrically-spread 6–7 km thickness (White et al., 2001). This uniform crustal
36 thickness is a result of efficient mantle melting and consistent melt extraction,
37 geochemically expressed by dilute incompatible element concentrations (Gale et al.,
38 2014). Hydrothermal vents, however, also exist on colder, slower-spreading centers with
39 lower mantle potential temperatures and thus lower extents of melting (Dalton et al.,
40 2014) and decreased, sporadic volcanism (Dick et al., 2003; Rubin and Sinton, 2007),
41 which produces heterogeneous crust (Fig. DR1). This crustal heterogeneity is most
42 pronounced along ridges that spread at ultraslow rates $< 20 \text{ mm yr}^{-1}$ (Dick et al., 2003)
43 with axial depths that are generally $> 4000 \text{ mbsl}$ (Dick et al., 2003). Though
44 hydrothermal vents on ultraslow-spreading centers have been found (e.g., Michael et al.,
45 2003), their abundance, distribution, and nature is relatively unknown.

46 Several vent fields along slow- (20–60 mm yr⁻¹) spreading centers, notably the
47 Lost City Field (e.g., Früh-Green et al., 2003) and the Rainbow Vent (e.g. Canales et al.,
48 2017) on the Mid-Atlantic Ridge have also been discovered in off-axis regions and/or
49 where volcanism is sparse. Though the role of magmatism in driving some types of
50 hydrothermal venting at these settings is uncertain, the amount of magmatism clearly
51 influences the seafloor morphology of off-axis vent localities, which can be either
52 symmetric or asymmetric about the central axis. Slow and ultraslow seafloor spreading
53 can switch between symmetric and asymmetric modes on a ~1–2 My timescale
54 (Tucholke et al., 2008), with the transitions caused by the change in ratio of magmatism
55 relative to tectonism (Buck et al., 2005). Symmetric seafloor develops when this ratio is
56 either very low or high. If magmatism is high, then the seafloor is characterized by high-
57 angle normal faults dipping toward the axis. In cases of extremely little magmatism,
58 which is common on ultraslow-spreading segments, the “smooth” seafloor develops as
59 predominantly mantle peridotite is exhumed (Cannat et al., 2003). When this magmatic-
60 tectonic ratio is low-to-moderate (~0.3-0.5), however, asymmetric ridge segments tend to
61 form as long-lived detachment faults exhume lower-crustal and/or upper-mantle rock,
62 forming oceanic core complexes (OCCs) (Olive et al., 2010).

63 Previous models have proposed that the death of an OCC is marked by an episode
64 of magmatism and generation of OCC-cutting high-angle faults (MacLeod et al., 2009).
65 This “life-cycle” of OCCs in turn affects the type of hydrothermal activity (McCaig et al.,
66 2007), though it is unclear if such venting is driven by deep magmatism (Allen and
67 Seyfried, 2004), serpentinization (Früh-Green et al., 2003) and/or lithospheric heat that is
68 channeled by deeply penetrating faults (Lowell et al., 2017). Moreover, if magmatism is

69 fluctuating around a lower average at ultraslow-spreading centers than at slow-spreading
70 centers (Rubin and Sinton, 2007), then the life cycle of OCCs at more magma-poor
71 ultraslow-spreading centers may differ from this model, where an increase in magmatism
72 causes an OCC-mode of seafloor spreading, and a decrease in magmatism marks the
73 death of the detachment fault. The Mid-Cayman Spreading Center (MCSC) plays a
74 special role in this discussion because it has been long-thought to be an and is an end-
75 member in axial depth, crustal thickness, and cold mantle potential temperature (Hayman
76 et al., 2011; Klein and Langmuir, 1987; ten Brink et al., 2002), yet it hosts at least two
77 hydrothermal vents, one of which sits on the summit of a large OCC (German et al.,
78 2010; Connelly et al., 2012). Here, we use recently acquired seismic data to help
79 constrain the development of the OCC and its hydrothermal vent, and evaluate the role of
80 magmatism in this process.

81 **THE MID-CAYMAN SPREADING CENTER AND THE VON DAMM VENT**

82 **FIELD**

83 The ~110 km-long MCSC is located between transform fault zones that separate
84 the Caribbean from the North American plate (Fig. 1), and accommodating a local
85 discrepancy in plate motion results in one of the slowest orthogonal rates (~15 mm yr⁻¹)
86 globally. In the central portion of the MCSC, an OCC named “Mt. Dent” (Edgar et al.,
87 1991) rises ~3 km from the adjacent axial rift, and the Von Damm Vent Field (VDVF)
88 was discovered near its summit in 2010 (Connelly et al., 2012). The Mt. Dent OCC is
89 quite mature in the sense of MacLeod et al. (2009), as shown by both the age range
90 across the OCC (likely 1.5-2 My) (Fig. DR10), and steep faults that cut the detachment
91 surface (Stroup and Fox, 1981). Additionally, a linear feature, potentially an axial-

92 volcanic ridge (AVR), cuts obliquely across the deep southern rift of the MCSC, trending
93 north-northwest directly into Mt. Dent. It has not been established whether this feature
94 has caused recent volcanism near or on Mt. Dent, though pillow basalts of unknown
95 provenance have been reported (Stroup and Fox, 1981; Van Dover et al., 2014). If so, the
96 AVR could signify the propagation of magmatism into the “dying” OCC (MacLeod et al.,
97 2009).

98 Ultramafic and mafic gabbroic rocks have been sampled around the VDVF and
99 along the adjacent detachment fault surface (Hayman et al., 2011; Stroup and Fox, 1981)
100 suggesting the OCC was magmatically constructed, but serpentinized peridotites have
101 also been sampled both near the termination of the detachment as well as areas to the
102 south (Fig. 1). Similarly, the ~200 °C, moderate-pH vent fluids have geochemical
103 compositions consistent with very long residence times in fractured crustal rocks
104 (McDermott et al., 2015), yet the high Mg concentrations, including the local
105 precipitation of talc, suggests a partly ultramafic, possibly mantle host (Hodgkinson et al.,
106 2015). Moreover, while emitting only moderate-temperature fluids, the heat flux is
107 similar to high-temperature vents associated with magmatism, but low H₂S
108 concentrations suggest nominal magmatic input (Hodgkinson et al., 2015). It therefore
109 remains unclear whether Mt. Dent is primarily a crustal or mantle dominated OCC and to
110 what extent magmatism is involved in driving the VDVF.

111 **CAYSEIS SEISMIC PROFILE ACROSS MT. DENT**

112 In order to determine the crustal and upper mantle structure beneath the VDVF,
113 we conducted the Cayman Seismic (CaySeis) experiment during April, 2015 aboard the
114 *F/S Meteor* (Cruise M115), a multi-national collaboration to collect wide-angle, ocean-

115 bottom seismic refraction and under way geophysical data of the MCSC. Through
116 tomographic inversion of P-wave first arrival times from the wide-angle refraction data
117 (Van Avendonk et al., 1998; Van Avendonk et al., 2001) (Supp. Methods), we produced
118 a 2D P-wave seismic velocity (V_p) profile along Line 2, which crosses the neovolcanic
119 zone, Mt. Dent, and the VDVF (Fig. 1). In the tomographic image (Fig. 2), the velocity
120 structure to the east and west of Mt. Dent is fairly homogenous with a steady change in
121 V_p from $\sim 3.5\text{--}4.0\text{ km s}^{-1}$ near the seafloor to $\sim 7.5\text{--}8.0\text{ km s}^{-1}$ at depths of $\sim 3\text{--}4\text{ km}$ below
122 the seafloor. In contrast, in the vicinity of Mt. Dent and the VDVF, near-surface V_p
123 reaches 6.0 km s^{-1} . Mt. Dent exhibits a $10\text{--}15\text{ km}$ by $\sim 3\text{ km}$ body with a V_p of nearly 6.5
124 km s^{-1} that dips $\sim 20^\circ$ upwards toward the west. Beneath this zone of high V_p at $4.0\text{--}7.0$
125 km below Mt. Dent, V_p is as low as $\sim 6.0\text{ km s}^{-1}$. At larger depth, V_p increases gradually
126 to 7.5 km s^{-1} at $\sim 9.5\text{ km}$ below the seafloor.

127 In our view, the high V_p (6.5 km s^{-1}) at shallow depth beneath Mt. Dent is best
128 explained by a gabbro body, or a dense cluster of gabbro bodies, that has not been
129 extensively altered and does not have many open fractures, based on observations in
130 similar settings (Canales et al., 2008). This high- V_p body is not likely composed of much
131 mantle peridotite because serpentinization near the surface would likely result in a V_p
132 well below the observed 6.0 km s^{-1} , nor can Mt. Dent host a thick basaltic section because
133 high-porosity basalt has a $V_p < 6.0\text{ km s}^{-1}$ (Christensen, 1996). In contrast, the 6.0 km s^{-1}
134 V_p at larger depths beneath the summit of Mt. Dent could be caused by either fluid-filled
135 fractures, high temperatures, or partial melt in either crustal or mantle rock, because the
136 V_p of gabbro and peridotite would otherwise be on the order of $> 6.0\text{ km s}^{-1}$ according to
137 widely used empirical relationships (Christensen, 1996). The gravity anomaly associated

138 with Mt. Dent is consistent with this interpretation as well, with the free air anomaly fit
139 well by a large low-density region (Fig. DR10). We return to the alternative
140 interpretations of this deeper zone of relatively low Vp in the following Discussion.

141 Immediately adjacent to Mt. Dent, on axis, there is no seismic evidence for a thick
142 (> ~1 km) layer of young igneous crust, as the Vp of the shallow lithosphere is ~3.5–4.0
143 km s⁻¹, high for young extrusive basalts, increasing with depth with a constant gradient to
144 a mantle Vp of 7.5–8.0 km s⁻¹ at ~5.0 km beneath the axis. The velocity gradient further
145 suggests that on-axis to the east of Mt. Dent there is currently little magmatism and low
146 temperatures persist. The velocity structure of the shallow basement to the west of Mt.
147 Dent and east of the MCSC is consistent with either thin volcanic crust and/or
148 serpentinized mantle, but due to the ambiguity of relating Vp to lithology, distinguishing
149 basalt from serpentinite requires alternative data sets. At depths of ~3.5–4.0 km below
150 the seafloor, Vp reaches 8.0 km s⁻¹, indicating unaltered mantle.

151 **DISCUSSION**

152 Given the new seismic velocity image of the axial valley and Mt. Dent (Fig. 2)
153 and the notion that the MCSC is subject, overall, to low extents of melting, we present
154 two alternative models for the formation and evolution of Mt. Dent (Fig. 3). Both invoke
155 the rolling hinge model (e.g., Lavier et al., 1999) wherein the inclined gabbro body, or
156 bodies, and overall lack of volcanic cover on Mt. Dent arises from flexural rotation of the
157 once steep detachment fault to shallow angles as the OCC was exhumed from beneath the
158 brittle-ductile transition (e.g. Hayman et al., 2011). Initially, magmatism in this central
159 portion of the MCSC was low and symmetric seafloor spreading produced either thin
160 crust or smooth, mantle-dominated seafloor. An increase in magmatism ~2 Mya along

161 this portion of the spreading center produced the gabbroic intrusion deep beneath the
162 axial valley (Fig. 3A), initiating an asymmetric period of seafloor spreading. During this
163 magmatic pulse, an eastwardly-dipping detachment fault began to exhume and rotate the
164 plutonic body from beneath the axial valley. Exhumation likely occurred most rapidly ~1
165 Mya, prior to the development of the central anomaly magnetic high on the eastern flank
166 of Mt. Dent (Fig. DR10). Basaltic crust that formed during this magmatic, asymmetric
167 phase was stripped from the OCC and is now preserved on the eastern flank of the
168 MCSC. Magmatism on axis has since waned and the gabbroic intrusion in Mt. Dent has
169 cooled.

170 We propose two alternate models to explain the seismic velocity structure and the
171 presence of the VDVF. In the first model (Fig 3B), the region of low V_p is interpreted as
172 a cracking front. During exhumation, Mt. Dent underwent faulting and fracturing in
173 response to flexure and uplift relative to the rift axis and faults and fractures propagated
174 through Mt. Dent. Once slip on the detachment fault ceased, continued tectonic extension
175 throughout Mt. Dent caused deep cracking, allowing for hydrothermal circulation and
176 initiating the VDVF. The cracking front under Mt. Dent defines an area at the base of the
177 lower crustal, now cooled, plutonic body. There, cracks can be transiently open so as to
178 feed the vent and cause the low- V_p zone, while fractures are mostly sealed in the high- V_p
179 gabbro body. Such transient opening and closing of cracks due to evolving
180 thermomechanical conditions is a central premise of many structurally controlled
181 hydrothermal systems (e.g., Sibson, 1990) and recent analytical modeling finds that deep
182 crustal faulting can drive moderate-temperature venting without magmatic input (Lowell
183 et al., 2017). If true, the heat of exhumation, along with heat from serpentinization

184 reactions of the peridotite in Mt. Dent, may be enough to fuel the VDVF. The “cracking
185 front” model is supported by the long hydrothermal fluid residence times and low
186 magmatic heat input required by the geochemistry of the vent fluids (Hodgkinson et al.,
187 2015).

188 The second model (Fig. 3B) interprets the low-Vp zone as elevated temperature or
189 partial melt, caused by off-axis magmatic intrusion into the deeper, ultramafic part of Mt.
190 Dent. This model would satisfy the argument that a magmatic heat source is necessary for
191 driving venting (Baker, 2009). The possible north-northwest trending AVR (Fig. 1)
192 intersects Mt. Dent near the VDVF, and a small episode of magmatism could intrude
193 magmatic sills into the base of the already-permeable Mt. Dent where Vp appears
194 depressed, driving the VDVF and causing local basaltic eruptions. We suggest, however,
195 that it is unlikely there is active magmatism and diking within Mt. Dent today, because
196 such magmatism would cause Vp deep in Mt. Dent to be lower and sampled by less rays.
197 Alternatively, there could be out-of-plane magmatism that could not be imaged by the 2-
198 D seismic line, leading to partially-molten sills in the OCC, as has been suggested for the
199 Rainbow vent on the MAR (Canales et al., 2017).

200 Ultraslow spreading centers are, in general, in remote parts of the globe, and thus
201 acquiring data to predict the conditions that favor VDVF-type vents *a priori* is highly
202 desirable. We argue that the fluctuation of magmatism that is typical of ultraslow-
203 spreading centers produces variable crustal thickness and plays a role in the life cycle of
204 the Mt. Dent OCC and its hydrothermal vent. Whether magmatism is needed to drive the
205 VDVF, however, is still in question. If the cracking front model is correct, then the death
206 of Mt. Dent was not marked by magmatism, but instead by a decrease in magmatism, as

207 might be predicted in a colder, less magmatic setting. If this sill intrusion model is
208 correct, however, then the death of Mt. Dent may have been caused by an episode of
209 magmatism within the OCC, and this may be a common feature among all OCCs. Further
210 modeling of how lithospheric heat could drive moderate temperature vents, or other data
211 sets in the MCSC, like seismic reflection data or higher resolution geophysical research,
212 could help elucidate this outstanding problem. If VDVF-type vents are common at
213 ultraslow-spreading centers, they would broaden the types of microbial, biological, and
214 chemical exchanges that occur in these environments.

215

216 **ACKNOWLEDGMENTS**

217 We thank the captain and crew of the *F/S Meteor*, the technicians of the NERC's
218 Ocean-Bottom Instrumentation Facility (OBIF (Minshull et al., 2005)), GEOMAR,
219 UTIG, and NEPA, including Steffen Sastrup, Anatoly Mironov, Cord Papenberg,
220 Mahshid Erfanian Mehr, Andrew Clegg, and Ben Pitcairn; We also thank NSF (OCE-
221 1356895), DFG, and NERC (NE/K011162/1) for funding this project. This is UTIG
222 contribution xxxx.

223 **REFERENCES CITED**

224 Allen, D.E., and Seyfried, W.E., 2004, Serpentinization and heat generation: constraints
225 from Lost City and Rainbow hydrothermal systems: *Geochimica et Cosmochimica*
226 *Acta*, v. 68, no. 6, p. 1347-1354. doi:10.1016/j.gca.2003.09.003.
227 Baker, E.T., 2009, Relationships between hydrothermal activity and axial magma
228 chamber distribution, depth, and melt content: *Geochemistry, Geophysics,*
229 *Geosystems*, v.10, no.6, doi:10.1029/2009gc002424

- 230 Buck, R.W., Lavier, L.L., and Poliakov, A.N.B., 2005, Modes of faulting at mid-ocean
231 ridges: *Nature*, v. 434, p. 719–723, doi:10.1038/nature03358.
- 232 Canales, J.P., Tucholke, B.E., Xu, M., Collins, J.A., and DuBois, D.L., 2008, Seismic
233 evidence for large-scale compositional heterogeneity of oceanic core complexes:
234 *Geochemistry Geophysics Geosystems*, v. 9, Q08002, doi:10.1029/2008GC002009.
- 235 Canales, J.P., Dunn, R.A., Arai, R., and Sohn, R. A., 2017, Seismic imaging of magma
236 sills beneath an ultramafic-hosted hydrothermal system: *Geology*. v. 25, no. 5, p.
237 451-454, doi:10.1130/G38795.1.
- 238 Cannat, M., Rommevaux-Jestin, C., and Fujimoto, H., 2003, Melt supply variations to a
239 magma-poor ultra-slow spreading ridge (Southwest Indian Ridge 61° to 69°E):
240 *Geochemistry Geophysics Geosystems*, v. 4, p. 9104, doi:10.1029/2002GC000480.
- 241 Christensen, N.I., 1996, Poisson's ratio and crustal seismology: *Journal of Geophysical*
242 *Research. Solid Earth*, v. 101, p. 3139–3156, doi:10.1029/95JB03446.
- 243 Connelly, D.P., et al., 2012, Hydrothermal vent fields and chemosynthetic biota on the
244 world's deepest seafloor spreading centre: *Nature Communications*, v. 3, p. 620,
245 doi:10.1038/ncomms1636.
- 246 Dalton, C.A., Langmuir, C.H., and Gale, A., 2014, Geophysical and Geochemical
247 Evidence for Deep Temperature Variations Beneath Mid-Ocean Ridges: *Science*,
248 v. 344, p. 80–83, doi:10.1126/science.1249466.
- 249 Dick, H.J.B., Lin, J., and Schouten, H., 2003, An ultraslow-spreading class of oceanic
250 ridge: *Nature*, v. 426, p. 405–412, doi:10.1038/nature02128.
- 251 Edgar, T. N., Dillon, W. P., Parson, L. M., Scanlon, K. M., Jacobs, C. L., and Holcombe,
252 T., L., 1991, GLORIA sidescan-sonar image and interpretation of the central

- 253 Cayman trough, northwestern Caribbean Sea, U.S. Geological Survey Miscellaneous
254 Field Investigations Map MF 2083-A: Reston, Virginia, United States Geological
255 Survey.
- 256 Früh-Green, G.L., Kelley, D.S., Bernasconi, S.M., Karson, J.A., Ludwig, K.A.,
257 Butterfield, D.A., Boschi, C., and Proskurowski, G., 2003, 30,000 Years of
258 Hydrothermal Activity at the Lost City Vent Field: *Science*, v. 301, p. 495–498,
259 doi:10.1126/science.1085582.
- 260 Gale, A., Langmuir, C.H., and Dalton, C.A., 2014, The Global Systematics of Ocean
261 Ridge Basalts and their Origin: *Journal of Petrology*, v. 55, p. 1051–1082,
262 doi:10.1093/petrology/egu017.
- 263 German, C.R., Bowen, A., Coleman, M.L., Honig, D.L., Huber, J.A., Jakuba, M.V.,
264 Kinsey, J.C., Kurza, M.D., Leroy, S., McDermott, J.M., Mercier de Lépinay, B.,
265 Nakamura, K., Seewald, J.S., Smith, J.L., Sylva, S.P., Van Dover, C.L., Whitcomb,
266 L.L., and Yoerger, D.R., 2010, Diverse styles of submarine venting on the ultraslow
267 spreading Mid-Cayman Rise: *Proceedings of the National Academy of Science*, v.
268 107, no. 14, p. 14,020-14,025. doi:10.1073/pnas.1009205107.
- 269 Hayman, N. W., Grindlay, N. R., Perfit, M. R., Mann, P., Leroy, S., and de Lépinay, B.
270 M., 2011, Oceanic core complex development at the ultraslow spreading Mid-
271 Cayman Spreading Center: *Geochemistry, Geophysics, Geosystems*, v. 12, Q0AG02,
272 doi:10.1029/2010GC003240.
- 273 Hodgkinson, M.R., Webber, A.P., Roberts, S., Mills, R.A., Connelly, D.P., and Murton,
274 B.J., 2015, Talc-dominated seafloor deposits reveal a new class of hydrothermal
275 system: *Nature Communications*, v. 6, p. 10150, doi:10.1038/ncomms10150.

- 276 Kelley, D.S., Baroos, J.A., and Delaney, J.R., 2002, Volcanoes, Fluids, and life at mid-
277 ocean ridge spreading centers: *Annual Review of Earth and Planetary Sciences*, v.
278 30, no. 1, p.385-491. doi:10.1146/annurev.earth.30.091201.141331.
- 279 Klein, E.M., and Langmuir, C.H., 1987, Global correlations of ocean ridge basalt
280 chemistry with axial depth and crustal thickness: *Journal of Geophysical Research*,
281 v. 92, p. 8089–8115, doi:10.1029/JB092iB08p08089.
- 282 Lavier, L., Buck, R.W., and Poliakov, A.N.B., 1999, Self-consistent rolling-hinge model
283 for the evolution of large-offset low-angle normal faults: *Geology*, v. 27, p. 1127–
284 1130, doi:10.1130/0091-7613(1999)027<1127:SCRHMF>2.3.CO;2.
- 285 Lowell, R.P., 2017, A fault-driven circulation model for the Lost City Hydrothermal
286 Field: *Geophysical Research Letters*. v. 44, doi:10.1002/2016GL072326.
- 287 MacLeod, C.J., Searle, R.C., Murton, B.J., Casey, J.F., Mallows, C., Unsworth, S.C.,
288 Achenbach, K.L., and Harris, M., 2009, Life cycle of oceanic core complexes: *Earth
289 and Planetary Science Letters*, v. 287, p. 333–344, doi:10.1016/j.epsl.2009.08.016.
- 290 McCaig, A.M., Cliff, R.A., Escartin, J., Fallick, A.E., and MacLeod, C.J., 2007, Oceanic
291 detachment faults focus very large volumes of black smoker fluids: *Geology*, v. 35,
292 no. 10, p. 935-938. doi:10.1130/g23657a.1.
- 293 McDermott, J.M., Seewald, J.S., German, C.R., and Sylva, S.P., 2015, Pathways for
294 abiotic organic synthesis at submarine hydrothermal fields: *Proceedings of the
295 National Academy of Sciences of the United States of America*, v. 112, p. 7668–
296 7672, doi:10.1073/pnas.1506295112.
- 297 Michael, P.J., Langmuir, C.H., Dick, H.J., Snow, J.E., Goldstein, S.L., Graham, D.W.,
298 Lehnert, K., Kurras, G.J., Jokat, W., Muhe, R., Edmonds, H.N., 2003, Magmatic and

- 299 amagmatic seafloor generation at the ultraslow-spreading Gakkel ridge, Arctic
300 Ocean: Nature, v. 423, p. 956-961. doi:10.1038/nature01704.
- 301 Olive, J.-A., Behn, M.D., and Tucholke, B.E., 2010, The structure of oceanic core
302 complexes controlled by the depth distribution of magma emplacement: Nature
303 Geoscience, v. 3, p. 491–495, doi:10.1038/ngeo888.
- 304 Rubin, K.H., and Sinton, J.M., 2007, Inferences on mid-ocean ridge thermal and
305 magmatic structure from MORB compositions: Earth and Planetary Science Letters,
306 v. 260, p. 257–276, doi:10.1016/j.epsl.2007.05.035.
- 307 Sibson, R.H., 1990, Conditions for fault-value behaviour. Geological Society, London,
308 Special Publications, v. 54, no. 1, p. 15-28. doi:10.1144/GSL.SP1990.054.01.02.
- 309 Stroup, J.B., and Fox, P.J., 1981, Geologic investigations in the Cayman Trough:
310 Evidence for thin crust along the Mid-Cayman Rise: The Journal of Geology, v. 89,
311 p. 395–420, doi:10.1086/628605.
- 312 ten Brink, U.S., Coleman, D.F., and Dillon, W.P., 2002, The nature of the crust under the
313 Cayman Trough from gravity: Marine and Petroleum Geology, v. 19, p. 971-987.
- 314 Tucholke, B.E., Behn, M.D., Buck, W.R., and Lin, J., 2008, Role of melt supply in
315 oceanic detachment faulting and formation of megamullions: Geology, v. 36, p. 455–
316 458, doi:10.1130/G24639A.1.
- 317 Van Avendonk, H.J.A., Harding, A.J., Orcutt, J.A., and McClain, J.S., 1998, A two-
318 dimensional tomographic study of the Clipperton transform fault: Journal of
319 Geophysical Research, v. 103, p. 17,885–17,899, doi:10.1029/98JB00904.
- 320 Van Avendonk, H.J.A., Harding, A.J., Orcutt, J.A., and McClain, J.S., 2001, Contrast in
321 crustal structure across the Clipperton transform fault from travel time tomography:

322 Journal of Geophysical Research, v. 106, p. 10,961–10,981,
323 doi:10.1029/2000JB900459.

324 Van Dover, C., Marsh, L., German C., John, B., Cheadle, M., Vacchione, M., Amon, D.,
325 Ball, B., Copley, J., Smary, C., Fuller, S.A., Phillips, B.T., Cantner, K., Auscavitch,
326 S., and Ballard, R.D., 2014, Exploration of the Mid-Cayman Rise, *Oceanography*, v.
327 27, p. 32-33.

328 White, R.S., Minshull, T.A., Bickle, M.J., and Robinson, C.J., 2001, Melt generation at
329 very slow-spreading oceanic ridges: Constraints from geochemical and geophysical
330 data: *Journal of Petrology*, v. 42, p. 1171–1196, doi:10.1093/petrology/42.6.1171.

331

332 FIGURE CAPTIONS

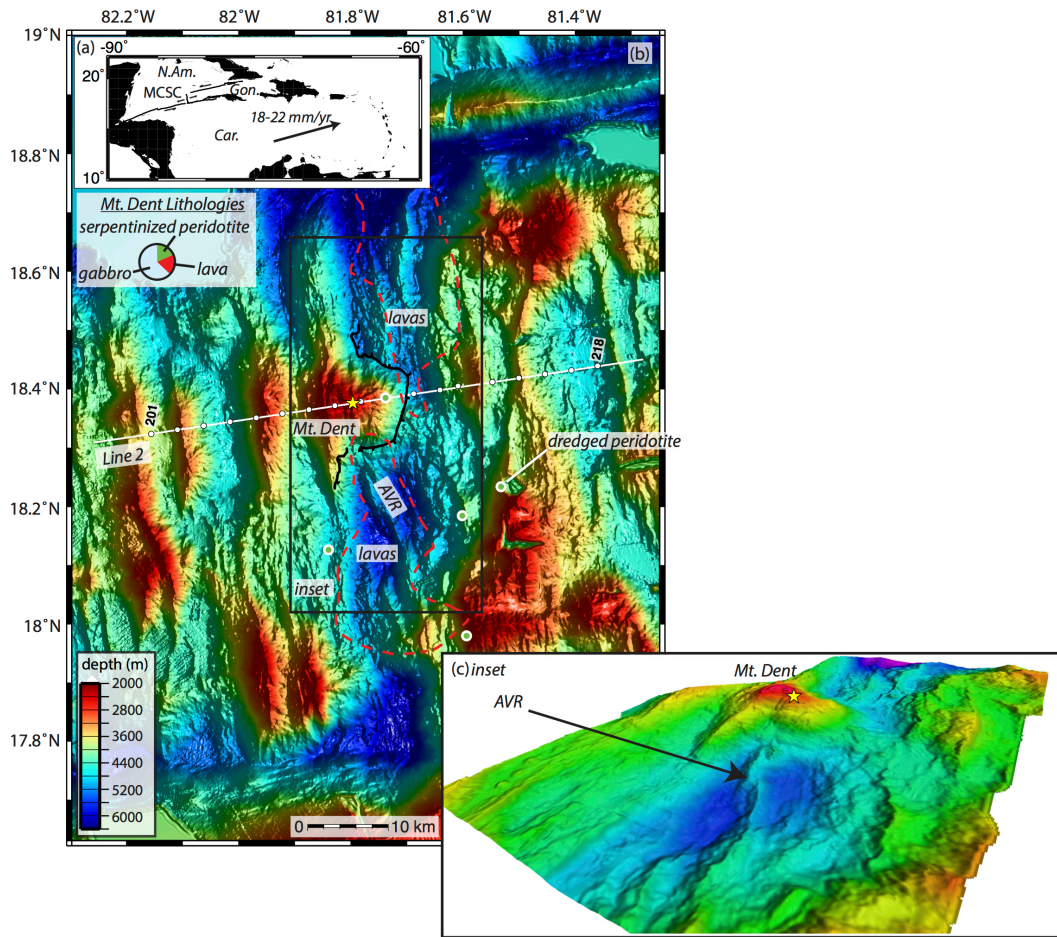
333

334 Figure 1. (A) Map and plate motions of the central Caribbean. (B) Bathymetric map of
335 the Mid Cayman Spreading Center area of interest. White line is seismic profile Line 2,
336 white circles are active-source ocean-bottom seismometer (OBS) stations, and the yellow
337 star is the Von Damm Vent Field (VDVF). Green dots are dredged peridotite samples,
338 and the red dashed lines encircle the areas that basaltic lavas have been dredged. Pie chart
339 reflects relative abundance of lavas, gabbro, and (variably serpentinized) peridotite in
340 dredges and dive samples from Mt. Dent (Hayman et al., 2011) (see key). The black
341 dashed line traces the Mt. Dent detachment fault. (C) Oblique view of Mt. Dent and the
342 possible axial volcanic ridge (AVR). The VDVF is marked by the yellow star.

343

344

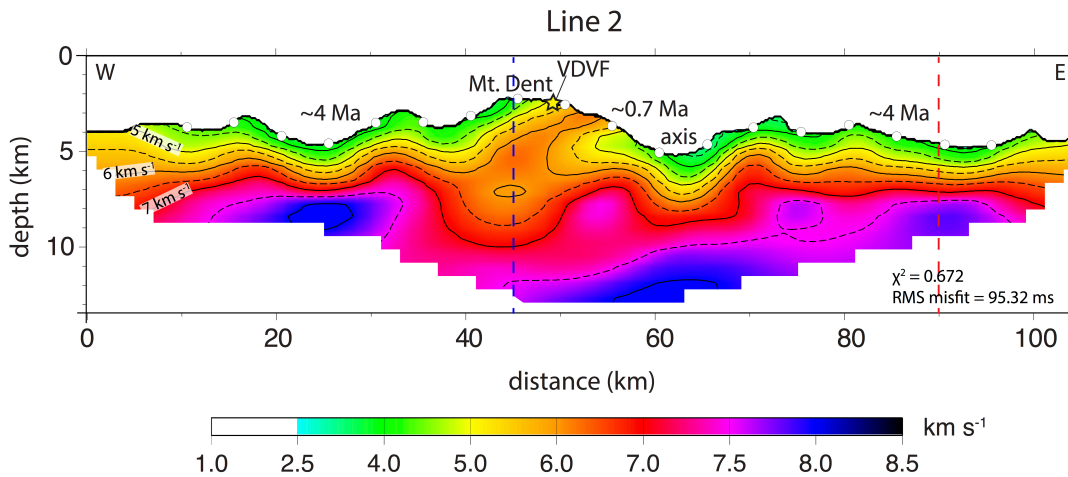
Jennifer L. Harding, Figure 1, Manuscript G39045



345

346 Figure 2. Compressional seismic velocity model of Line 2 derived from wide-angle
347 refraction data collected during the CaySeis experiment, at 2x vertical exaggeration.
348 Solid lines are velocity contours of 1 km s^{-1} with dashed lines every 0.5 km s^{-1} . The
349 yellow star denotes the location of the Von Damm Vent Field (VDVF). Approximate
350 seafloor ages from identified magnetic lineations are labeled. Red and blue dashed lines
351 correspond to 1-D profiles in Fig. DR5.
352

Jennifer L. Harding, Figure 2, Manuscript G39045



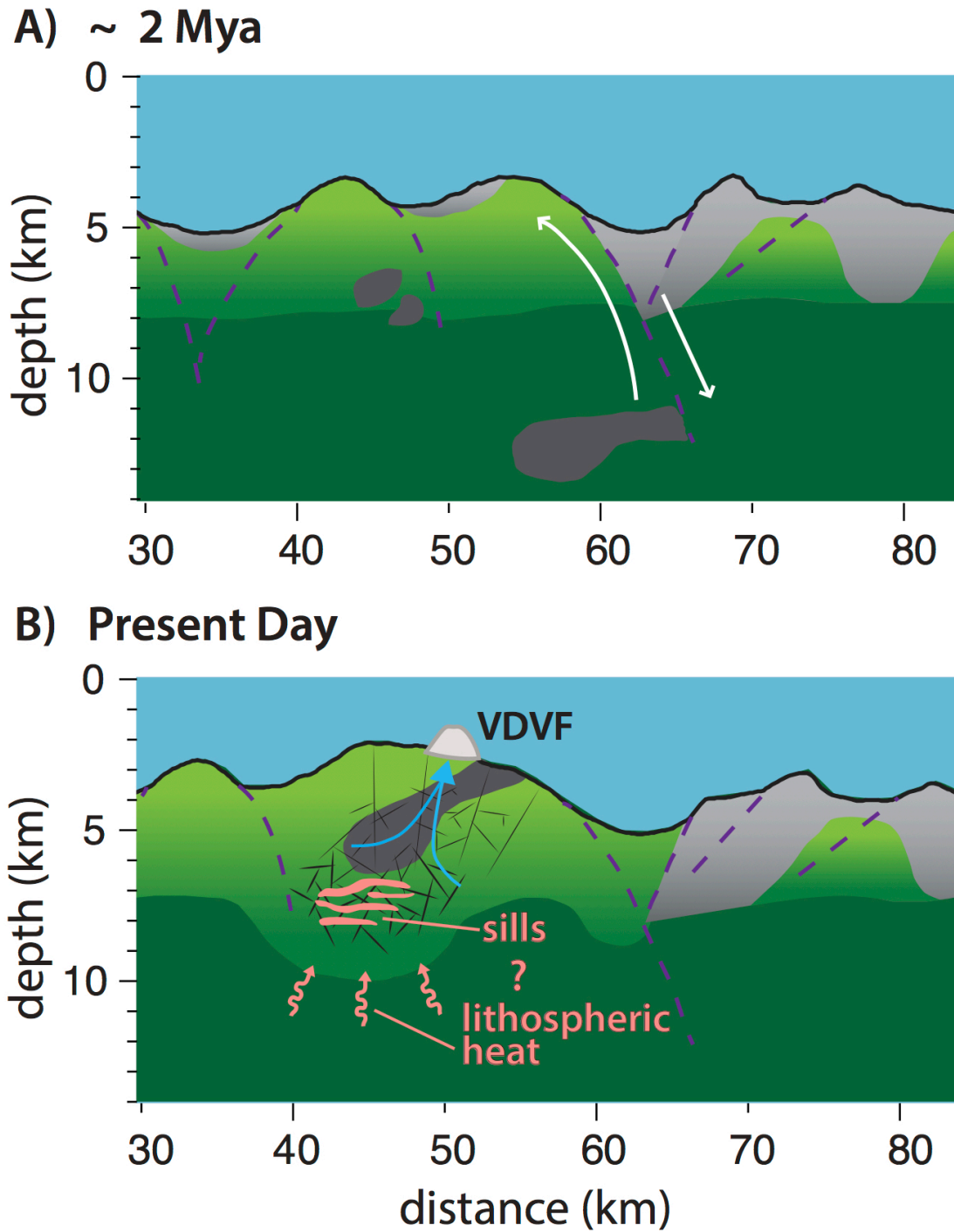
353

354
355 Figure 3. Evolution of Mt. Dent. (A) Axial region of the Mid-Cayman Spreading Center
356 (MCSC) along Line 2 at ~2 Mya. A gabbro (dark gray) body was produced on axis and
357 the detachment fault began slipping. Basaltic cover (light gray) to the east fluctuates with
358 seafloor spreading mode. Mantle peridotite (dark green) is increasingly serpentinized
359 (light green) with shallower depths. (B) Present-day axial region of the MCSC along Line
360 2. The gabbro body has been exhumed and rotated in the footwall of the detachment
361 fault, which has formed the oceanic core complex (OCC) Mt. Dent. Mt. Dent has been
362 fractured and faulted (black lines) as magmatism decreased and extensional stress on the
363 OCC increased, allowing for deep hydrothermal fluid circulation (possible path in blue
364 arrows). The heat source driving venting is either magmatic sill intrusions, or lithospheric
365 heat (light red).

366

367

Jennifer L. Harding, Figure 3, Manuscript G39045



370
371 1GSA Data Repository item 2017G39045, including a description of methods,
372 Supplementary Figures DR1-DR10, Table DR1, caption for database DR1 as well as
373 Database DR1, and an Excel file (Moho_compilation.zip) containing oceanic crustal
374 thickness data, is available online at <http://www.geosociety.org/datarepository/2017/> or
375 on request from editing@geosociety.org.

376

377

378

379 **Supplementary Materials for:**

380 **Magmatic-tectonic conditions for hydrothermal venting on**
381 **an ultraslow-spread oceanic core complex**

382 **J.L. Harding^{1*}, H.J.A. Van Avendonk¹, N.W. Hayman¹, I. Grevemeyer², C. Peirce³,**
383 **A. Dannowski²**

384 **correspondence to: jharding@utexas.edu**

385

386 **This PDF file includes:**

387 Methods

388 Figs DR1 to DR10

389 Table DR1

390

391 **Methods**

392 Na8.0 Compilation

393 The concentrations of incompatible element Na were compiled from basalts at
394 different spreading segments around the globe with different spreading rates (2). Na8.0
395 values are normalized to a MgO wt % of 8.0 using liquid-line of descent models (2).
396 Na8.0 values from locations close to hot spot influence, in particular the Afar, Iceland
397 and Samoa hotspots. These values are plotted vs. segment spreading rate as a red cloud
398 (Fig. DR1), as well as data points with error bars are plotted (Fig DR2).

399

400 Oceanic Crustal Thickness Compilation

401 Oceanic crustal thicknesses determined from over 200 seismic refraction studies
402 were compiled with spreading rate and seafloor age extracted for each data point using
403 isochrones (Müller et al., 2008) (see Database DR1). Data points were excluded from the
404 compilation if they were influenced by hot spots or fracture zones. Crustal thickness vs.
405 spreading rate is plotted as a blue cloud (Fig. DR1) and as data points with error bars
406 (Fig. DR3), excluding data collected before 1970 and from seafloor older than 20 Ma.

407

408 Seismic Tomography

409 We used active-source ocean-bottom seismometer (OBS) data collected along
410 Line 2 (Fig. 1) during the CaySeis cruise to produce the P-wave seismic velocity image
411 (Fig. 2). An airgun array of 12 G-guns with a total volume of 84 liters was towed behind
412 the *F/S Meteor*, producing seismic energy that was recorded by OBSs on the seafloor
413 between 4 to 20 Hz. These OBSs were pooled from three institutions, the University of

414 Texas Institute for Geophysics in Austin, Texas, the NERC's Ocean-Bottom
415 Instrumentation Facility in the UK, and the GEOMAR Centre for Ocean Research in
416 Kiel, Germany. OBSs were spaced ~ 5 km apart along the seafloor, with shots every
417 minute (~ 150 m shot spacing). A total of 18 OBSs comprise Line 2.

418 P-wave first arrival times were first picked from the wide-angle refraction data
419 collected by each OBS (Fig. DR4). Phases were not distinguished due to the rough
420 bathymetry and complicated structure of the Mid-Cayman Spreading Center (MCSC).
421 These picked times were assigned an error from 50 to 200 ms based on signal to noise
422 ratio and offset. These times were then inverted for P-wave velocities throughout a 106 x
423 25 km model space (Van Avendonk et al., 1998; Van Avendonk et al., 2001).
424 Additionally, multiple refractions were picked and incorporated into the inversion in
425 order to improve imaging of distal areas of the model space. These multiples represent P-
426 wave refractions with an additional bounce in the water column above the OBS.

427 The tomographic inversion process begins with a starting seismic velocity model
428 based on assumptions of oceanic crustal velocity structure (Fig. DR5). The raypaths from
429 all source-receiver pairs were calculated through the starting model using a hybrid
430 shortest path and raybending method (Van Avendonk et al., 2001) in a 3D (extended ± 1.6
431 km perpendicular to Line 2) model space to account for the rough bathymetry. The
432 difference between the picked P-wave travel times and calculated travel times are then
433 inverted for seismic velocities everywhere in the model space using a linearized least-
434 squares approach (Van Avendonk et al., 1998; Van Avendonk et al., 2001). This process
435 of calculating raypaths in the new model and then producing a new velocity model with a
436 least squares inversion is repeated until a minimum data misfit is achieved. In 9

437 iterations, the residual mean data fit reduced from 672 ms to 95 ms and the chi-squared
438 reduced from 44.53 to 0.67.

439 The iterative nonlinear tomographic inversion converged on two solutions that
440 both achieve a good data fit. These two solutions differ in the nature of the low-velocity
441 zone beneath Mt. Dent, to which the raypaths appear to be sensitive. To account for this,
442 we averaged 12 seismic velocity models from consecutive iterations of the inversion
443 passed the 9th iteration that produced an acceptable data misfit. This average represents
444 our final, preferred velocity model, with a residual mean data misfit of 95 ms and a chi-
445 squared of 0.67. Fig. DR6 shows the final seismic tomographic image with picked and
446 calculated travel times. The standard deviation of the final model (using the 12 inversion
447 results) was calculated (Fig. DR7). A resolution test was also carried out in order to show
448 how well the final velocity model resolves a body that is 10 km-wide by 5 km-high (Fig.
449 DR8). Table S1 summarizes the errors for all 18 OBSs.

450

451 Gravity

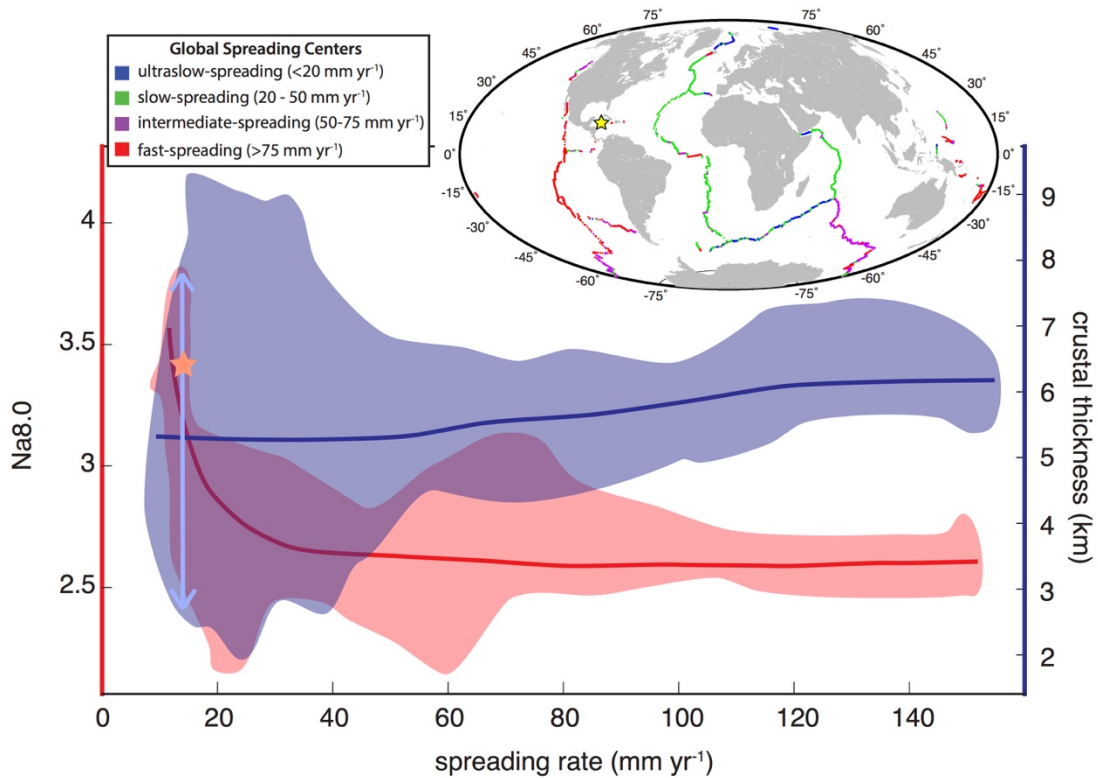
452 The shipboard gravity data were corrected to the Free-air Anomaly (FAA) (Fig.
453 DR10, middle panel). This FAA was then modeled for density in the center portion of
454 Line 2 where seismic control is best. Starting with velocity contours from the velocity
455 model, four layers were defined: a water layer, an upper crustal layer, a lower crustal
456 layer, and an upper mantle layer. These layers were then assigned densities and then
457 forward modeled to match the FAA (Fig. DR10, bottom panel). The water layer has a
458 density of 1.03 g cm^{-3} , the upper crustal layer has a density of 2.55 g cm^{-3} , the lower
459 crustal layer has a density of 2.65 g cm^{-3} , and the upper mantle layer has a density of 3.33

460 g cm⁻³. This modelling shows that Mt. Dent has relatively lower densities than the
461 surrounding lithosphere to the east and west.

462 Magnetics

463 The summit of Mt. Dent is ~14 km east of the center of the MCSC, ~2 my of
464 spreading judging by the long-term ~7.5 mm/yr half-rate, based primarily on magnetic
465 anomaly 3A, 5A and 6, all in off-axis crust >5 Ma-old (Leroy et al., 2000). The
466 protracted evolution of the Mt. Dent OCC is indicated by the edge of the central magnetic
467 anomaly along its eastern edge and an older positive magnetic anomaly along its western
468 edge (Fig. DR10, top panel) (Hayman et al., 2011). The ultraslow spreading rate renders
469 the exact ages of these anomalies unclear, but we take the older edge of the central
470 anomaly to be ~0.71 Ma and the youngest age of the next oldest positive anomaly to be
471 the edge of anomaly 2A, ~3.3 Ma (Leroy et al., 2000).

472

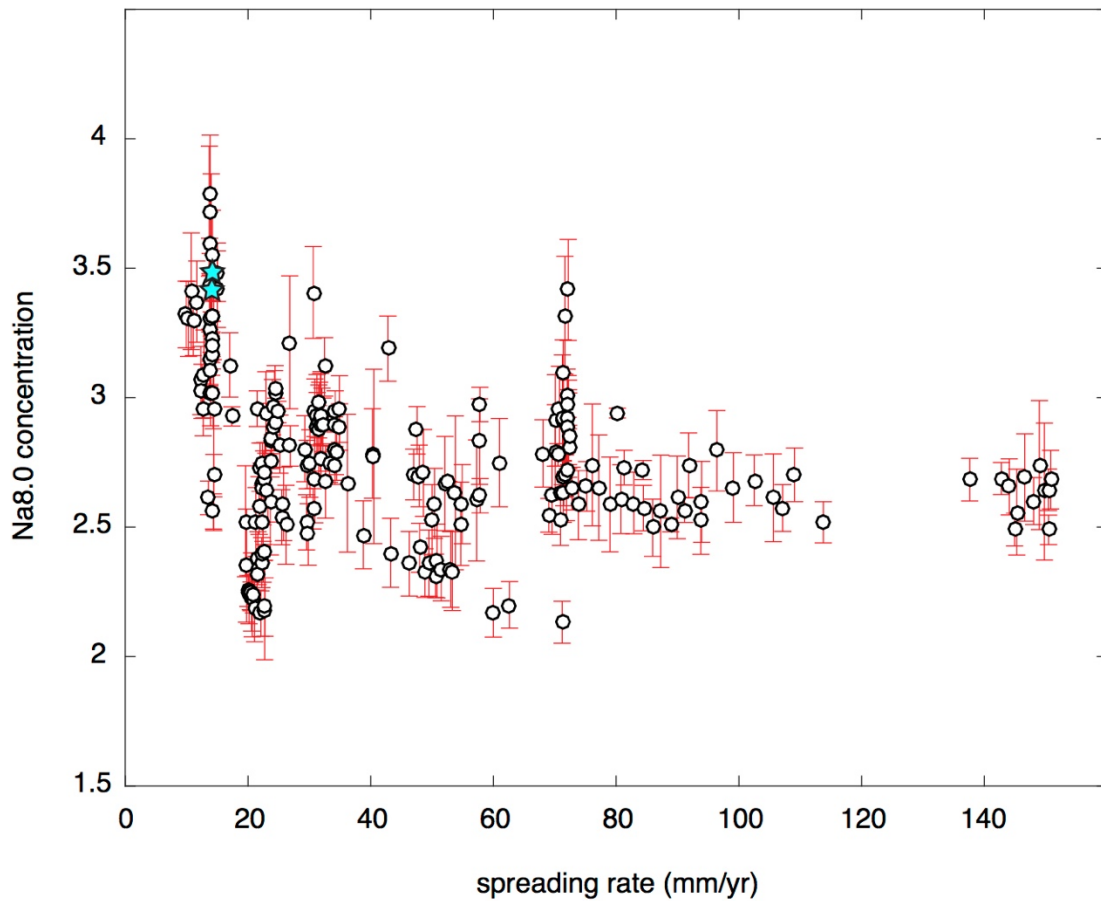


473
474

Fig. DR1:

475 Left-hand Y-axis is Na8.0 for segments of different spreading rate, incompatible element
476 Na normalized to an MgO of 8.0 Wt. % in liquid-line-of descent models (Gale et al.,
477 2014). Inset shows the location of the Mid-Cayman Spreading Center (MCSC) (yellow
478 star) and several other ultraslow spreading systems in a global view. Crustal thickness
479 values (right-hand Y-axis) are from a new compilation of seismic refraction studies
480 conducted in the last 40 years. The plot illustrates that at spreading centers far from
481 mantle plumes, incompatible elements become enriched and crustal thickness becomes
482 more variable as a result of low extents of mantle melting when spreading rate drops to <
483 20 mm yr⁻¹ (Dalton et al., 2014). The MCSC is important in this compilation because it
484 has some of the highest Na8.0 concentrations (red star), and previously reported lowest

485 crustal thickness values; as we show here the MCSC has highly variable crustal thickness
486 over time (light blue line) (Fig. DR3).
487

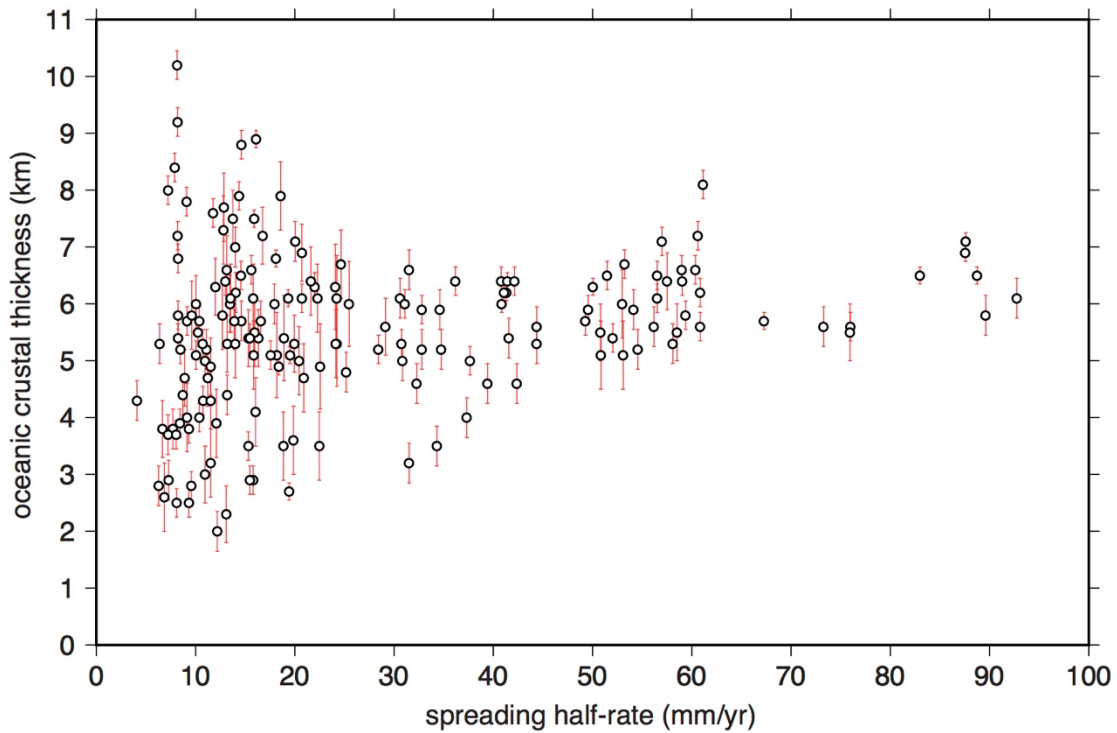


488

489 **Fig. DR2**

490 Na_{8.0} of basalts from segments of different spreading rates, where Na is normalized to an
491 MgO of 8.0 Wt. % in liquid-line-of descent models (Gale et al., 2014). Data near hotspots
492 were excluded from this plot. Mid-Cayman Spreading Center (MCSC) data is denoted by
493 the cyan stars. At spreading rates slower than $\sim 20 \text{ mm yr}^{-1}$, Na_{8.0} concentrations sharply
494 increase, suggesting less mantle melting at ultraslow-spreading centers such as the
495 MCSC.

496



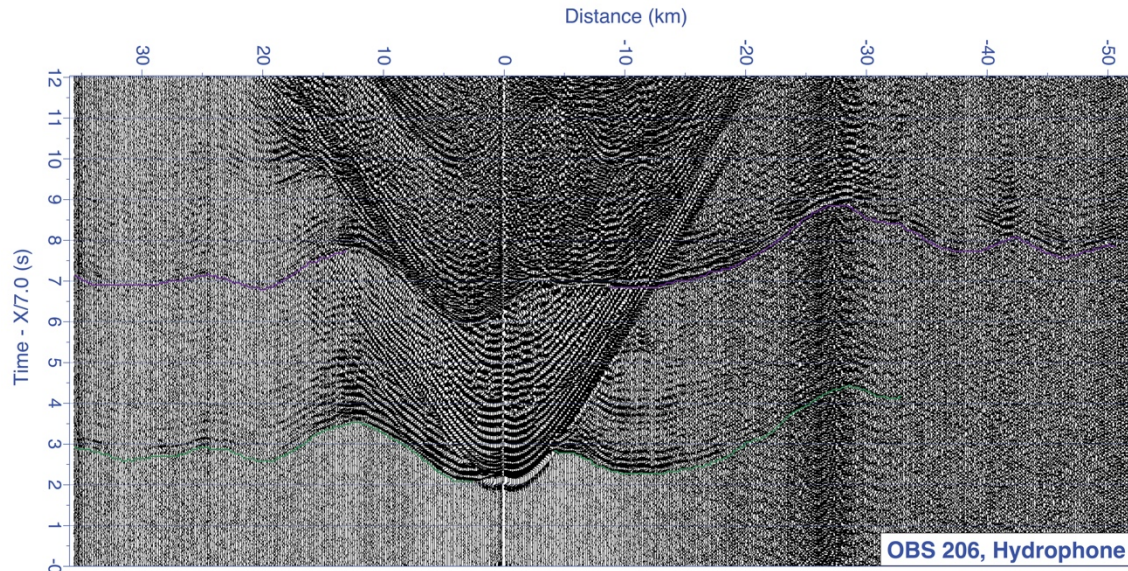
497

498 **Fig. DR3**

499 Oceanic crustal thickness vs. spreading half-rate from a compilation of seismically-
500 determined oceanic crustal thicknesses. Crustal thickness estimates included are of
501 oceanic crust younger than 20 Ma, collected since 1970, and away from hot spots or
502 fracture zones. This database is included as a separate file (Database DR1). Oceanic
503 crustal thickness averages ~ 6.0 km for spreading half-rates above 50 mm yr^{-1} , with
504 crustal thickness decreasing slightly for slower spreading rates. A significant change in
505 variability of crustal thickness can be observed at spreading half-rates lower than 50 mm
506 yr^{-1} , showing that ultraslow-spreading centers like the Mid-Cayman Spreading Center
507 behave differently from faster spreading centers.

508

509

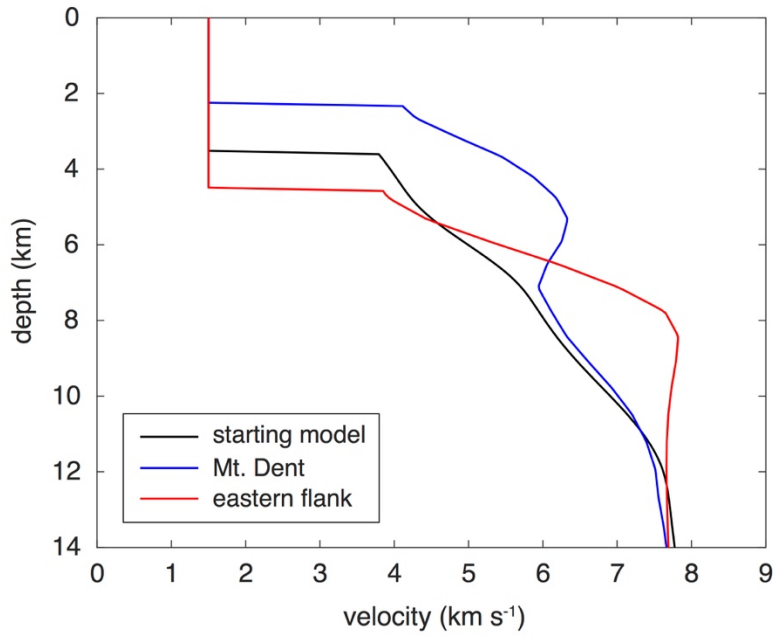


510
511

Fig. DR4

512 Wide-angle refraction data from the hydrophone channel of OBS 206, plotted as time at a
513 reduction velocity of 7 km s^{-1} , and band-pass filtered between 5-15 Hz. The first-arrival
514 P-wave travel-time picks are shown as green lines and the multiple P-wave picks are
515 shown as purple lines.

516



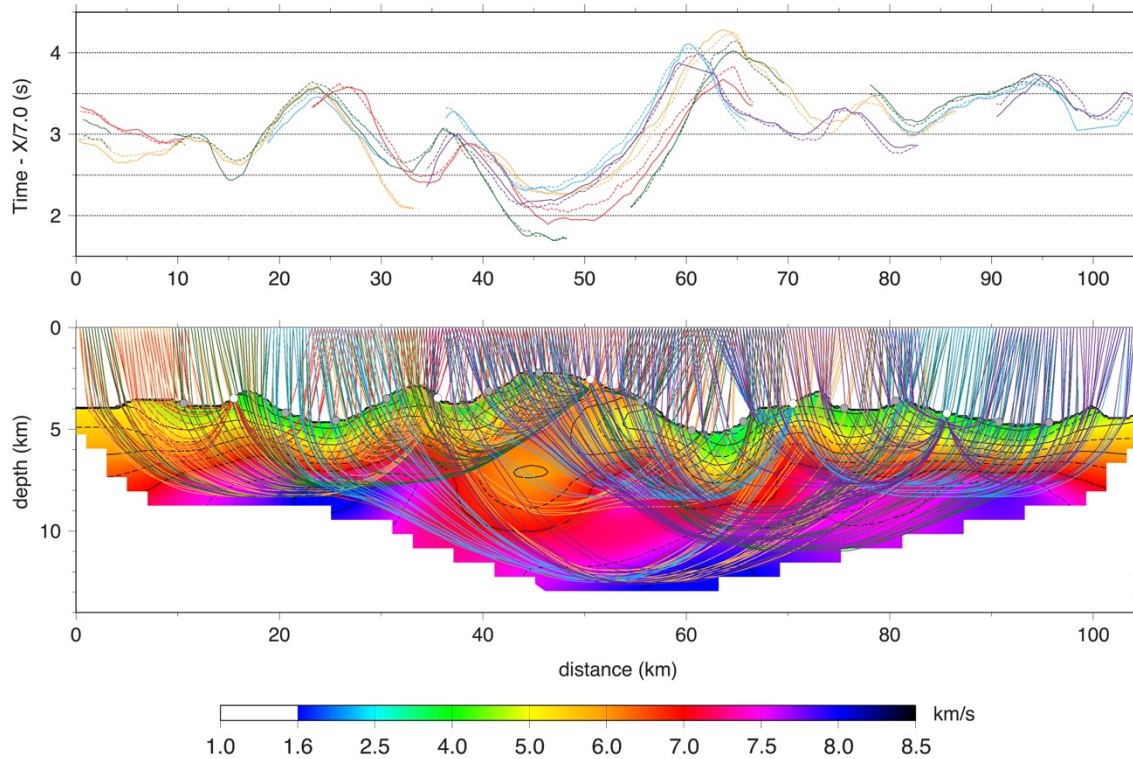
517

518 **Fig. DR5**

519 Velocity-depth profiles of the starting velocity model (black), Mt. Dent (red), and the
520 eastern flank (blue), which correspond to the dotted lines in the bottom panel of Fig. S4.

521

522



523

524 **Fig. DR6**

525 Raytracing diagram for the final seismic velocity model for Line 2. Top panel shows the

526 picked (solid lines) and calculated (dashed lines) P-wave travel times, including

527 multiples, plotted at a reduction velocity of 7 km s^{-1} , along Line 2. Colors indicate

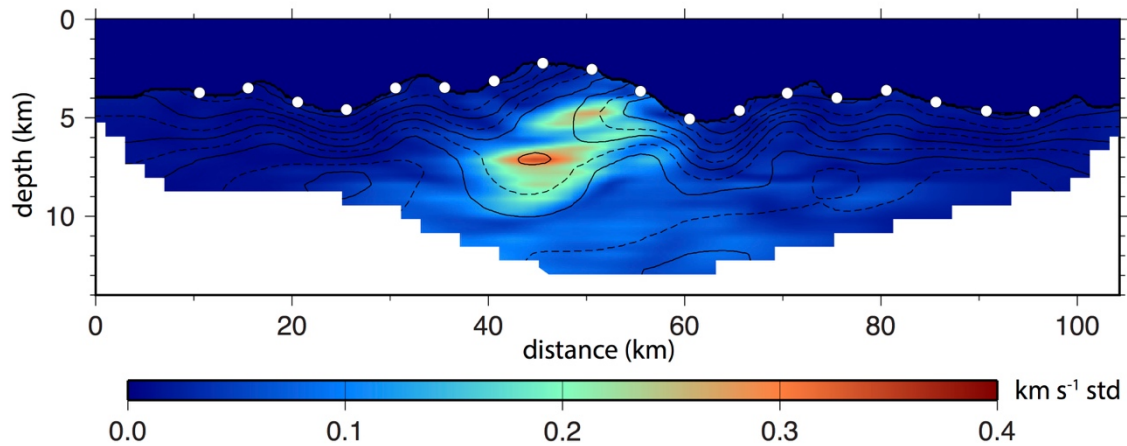
528 different OBSs that recorded these arrivals, which correspond to the bottom panel. The

529 bottom panel shows the final seismic velocity model at 2x vertical exaggeration with

530 raypaths for six different OBSs: 202 (red), 206 (orange), 209 (green), 213 (cyan), and 216

531 (purple).

532



533

534 **Fig. DR7**

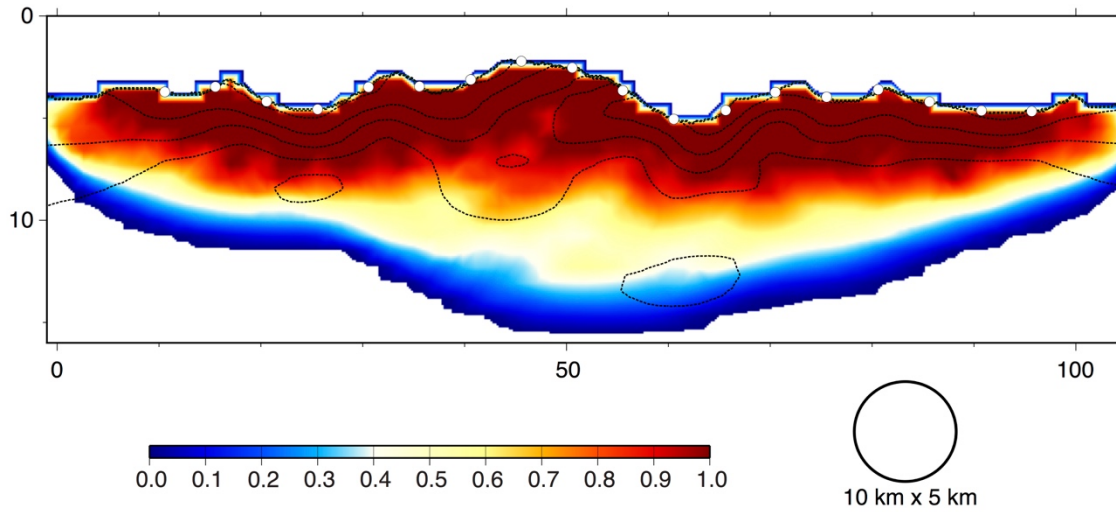
535 Standard deviation of the final seismic tomographic model at 2x vertical exaggeration.

536 White circles are OBS locations. Standard deviations range from 0 to 0.4 km s⁻¹. Most

537 standard deviations are < 0.1 km s⁻¹, showing that the final model is stable; differences

538 below Mt. Dent arise from the sensitivity of raypaths near the low velocity zone.

539



540

541 **Fig. DR8**

542 Line 2 resolution test for a 10 km-wide and 5 km-high body, plotted at 2x vertical
543 exaggeration. A value of 1 (red) indicates full resolution of a body this size and a value of
544 0 (blue) means a body of this size cannot be resolved. OBSs are shown as white circles.

545

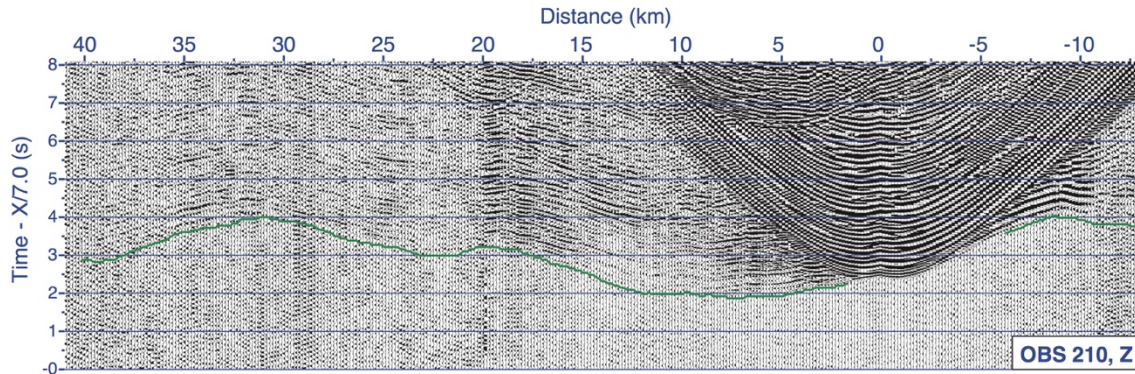
546 *Table DRI:*

547

OBS	Number of picks	Mean of travel-time residual (ms)	RMS misfit (ms)	Chi-squared
201	194	-24	78	0.583
202	168	-61	101	0.519
203	246	5	69	0.298
204	229	-5	58	0.424
205	183	-7	102	0.789
206	258	23	70	0.413
207	287	-69	88	0.735
208	218	-54	91	0.750
209	250	-8	88	0.628
210	143	145	198	3.017
211	295	7	58	0.370
212	255	101	151	0.831
213	202	-39	83	0.497
214	287	13	101	0.568
215	238	-37	74	0.583
216	201	8	79	0.959
217	185	29	89	0.472
218	73	76	108	0.586

548

549

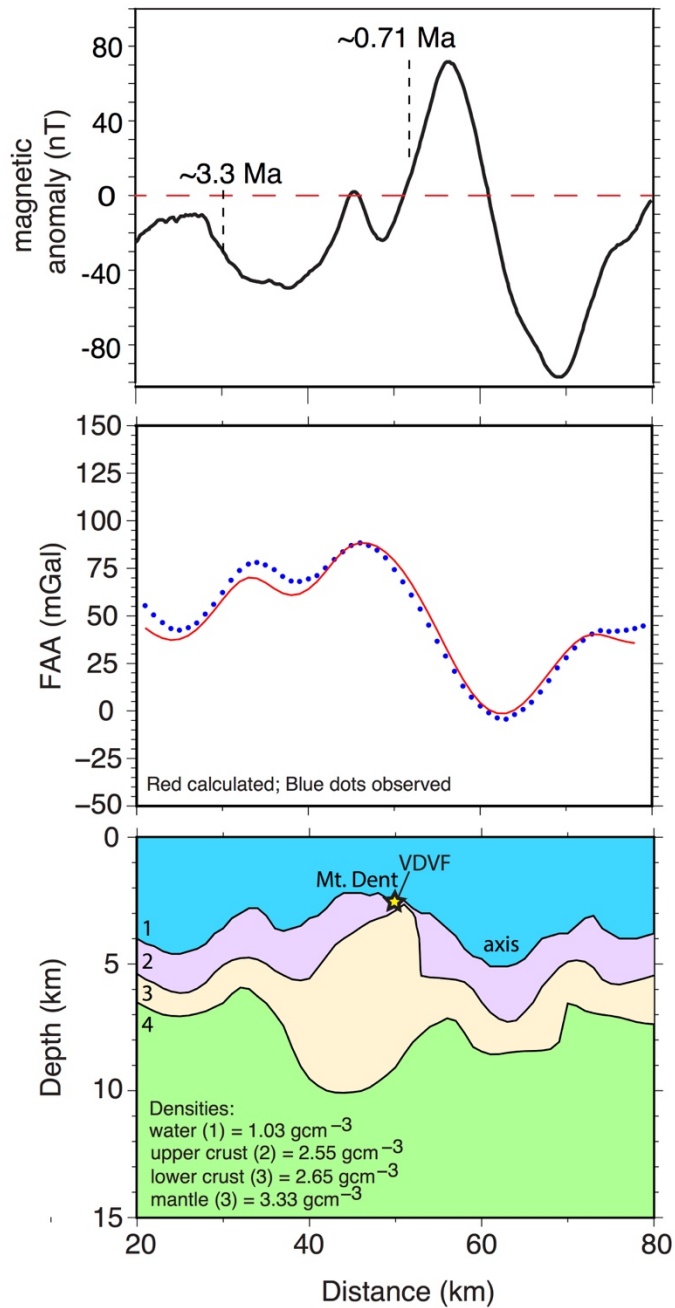


550
551

552 **Fig. DR9**

553 Wide-angle refraction data from the Z channel of OBS 210, plotted as time at a reduction
554 velocity of 7 km s^{-1} , and band-pass filtered between 5-15 Hz. The first-arrival P-wave
555 travel-time picks are shown as green lines and no multiple P-wave were picked for this
556 instrument.

557



558

559 **Fig. DR10**

560 Top panel shows the shipboard gravity from Line 2, and the magnetic anomalies over the

561 Mt. Dent detachment fault labeled with approximate reversal ages (Hayman et al., 2011).

562 Middle panel shows the Free-air Anomaly (FAA) (blue dots) compared with the

563 calculated FAA from density modelling (red line). Bottom panel shows the density model
564 to produce the calculated FAA. The density model consists of (1) a water layer of density
565 1.03 g cm^{-3} , (2) an upper crustal layer of density 2.55 g cm^{-3} , (3) a lower crustal layer of
566 density 2.65 g cm^{-3} , and (4) an upper mantle layer of density 3.33 g cm^{-3} . The gravity
567 modelling shows that Mt. Dent has lower-crustal densities with a deep crustal root.

568

569 ADDITIONAL REFERENCES:

570 Leroy, S., Mauffret, A., Patriat, P., and Mercier de Lepinay, B., 2000, An alternative
571 interpretation of the Cayman trough evolution from a reidentification of magnetic
572 anomalies: *Geophysical Journal International*, v. 141, p. 539-557.
573 doi:10.1046/j.1365-246x.2000.00059.x

574 Müller, R.D., Sdrolias, M., Gaina, C., and Roest, W.R., 2008, Age, spreading rates, and
575 spreading asymmetry of the world's ocean crust: *Geochemistry, Geophysics,*
576 *Geosystems*, v. 9, no.4, doi:10.1029/2007/gc001743.

577